

Multilaser Herriott cell for planetary tunable laser spectrometers

Christopher G. Tarsitano* and Christopher R. Webster

Jet Propulsion Laboratory, California Institute of Technology, 4800 Oak Grove Drive, Pasadena, California 91109, USA

*Corresponding author: christopher.g.tarsitano@aero.org

Received 17 August 2006; revised 25 July 2007; accepted 6 August 2007;
posted 7 August 2007 (Doc. ID 74199); published 24 September 2007

Geometric optics and matrix methods are used to mathematically model multilaser Herriott cells for tunable laser absorption spectrometers for planetary missions. The Herriott cells presented accommodate several laser sources that follow independent optical paths but probe a single gas cell. Strategically placed output holes located in the far mirrors of the Herriott cells reduce the size of the spectrometers. A four-channel Herriott cell configuration is presented for the specific application as the sample cell of the tunable laser spectrometer instrument selected for the sample analysis at Mars analytical suite on the 2009 Mars Science Laboratory mission. © 2007 Optical Society of America

OCIS codes: 080.2730, 080.2740, 120.6200, 300.6190, 350.6090.

1. Introduction

A. Planetary Gas Sampling Using Tunable Laser Spectroscopy

Tunable laser absorption spectroscopy is widely recognized as a direct, noninvasive, simple measurement technique that is known for its high sensitivity (subparts in 10^9) and specificity [1]. Using wavelength-modulation techniques, minimum detectable absorptions as small as two parts in 10^6 are possible, with two parts in 10^5 readily achieved in flight experiments. For reasonable path lengths, this translates to parts in 10^9 sensitivities for numerous species in the mid-IR, and tens of parts in 10^9 in the near-IR region. (These numbers depend specifically on the gas and conditions of interest.)

The Mars atmosphere is ideally suited to tunable laser spectroscopy because of its low atmospheric pressures (several millibars) and benign environment (moderately low temperatures and CO_2 as its primary component with small changes in the vertical pressure profile). Both Titan and Venus have chemically rich atmospheres that are best accessed in the mid-IR region but present harsh environmental conditions, with rapidly changing pressure profiles.

Ruggedness and reliability are key qualities needed for *in situ* spectrometers that must measure a variety of chemical species in photochemically active atmospheres containing hydrocarbon haze (Titan) or high-pressure, sulfuric acid environments (Venus).

The technology development of continuous-wave (cw) tunable laser sources suitable for planetary spectrometers has been impressive, with new devices available that work at “room temperature” or at temperatures accessible by thermoelectric (TE) coolers, typically temperatures above ~ 220 K. In the near-IR, TE-cooled tunable diode lasers (TDL) are available that have single-mode operation and output powers of 5–50 mW. These near-IR TDLs are suitable for probing transitions of atmospheric molecules with strong IR absorption cross sections such as CO_2 and H_2O . The increased optical powers emitted by the near-IR TDLs aid in the detection of atmospheric species with smaller absorption cross sections. The higher optical output powers not only increase the signal strength of the atmospheric species but allow for a larger path-length multipass cell.

Quantum cascade (QC) lasers, developed by Faist *et al.* in 1994 [2], are a revolutionary new semiconductor laser operating in the mid-IR region. Emission in a normal semiconductor laser occurs when an electron in the conduction band decays to a hole in the valence band. The frequency of the emission is determined by the bandgap. In contrast, QC lasers rely on

electrons cascading down a series of steps (active region) within the conduction band, where each step in the lattice is grown using molecular beam epitaxy. In principle, a photon is produced for every period of the structure. The frequency of the emission is determined by the energy levels within the wells of the active regions.

Using distributed feedback (DFB), a QC-DFB laser with single-mode emission had a side-mode suppression ratio of greater than 30 dB [3]. At room temperature (300 K), the QC-DFB laser operated in a pulsed mode with peak output powers of 60 mW. In cw operation, these earlier lasers produced an output power of approximately 10 mW at 120 K. Recent advances in QC laser technology has increased both the operating temperature and output power for cw operation. At room temperature (298 K), a QC laser operating in cw mode produced an optical output power of over 480 mW [4]. For a QC-DFB laser operating in cw mode, maximum emitted powers of 135 and 168 mW were obtained at temperatures of 298 and 288 K, respectively [5].

Interband cascade (IC) lasers are a relatively new type of semiconductor laser [6,7]. The periodic structure of an IC laser consists of an active region followed by an injection region. The active region contains a pair of coupled quantum wells. Emission of a photon occurs when an electron in the conduction band of the active region relaxes to a hole state in the valence band of the active region. The wavelength of the emission can be tailored by adjusting the energy levels of the active region via changing the layer thickness and composition. In addition, photon relaxation does not diminish the radiative efficiency of the IC laser as it does in the QC laser. Single-mode emission using IC-DFB lasers exhibits a side-mode suppression ratio of greater than 30 dB at 175 K [8]. Narrow mesa stripe IC lasers operate at temperatures of 237 and 350 K for cw and pulsed mode operation, respectively [9]. Recently, cw operating temperatures of 257 and 264 K have been reported for mid-IR IC lasers [10,11].

For all planetary missions, available spacecraft resources (mass, power, volume, cost) and reliability are driving restrictions, especially for nonorbiting measurements. For *in situ* gas measurements using mass spectrometers or tunable laser spectrometers, available platforms such as balloons, aircraft, surface and entry probes, and landed rovers present severe limitations on the available resources, with stringent requirements on operating environments. For typical Mars missions, *in situ* laser or mass spectrometers must have total masses typically 2–3 kg, draw less than ~30 W (all instruments including heaters), occupy 1–3 l (volume), and be able to endure severe temperature excursions (–30 to +60 °C). In addition, planetary protection requirements often mean that the instrument has to survive bakeouts for hours at 125 °C, at least prelaunch. The planetary protection requirements are to protect against cross contamination of the solar system bodies for future exploration.

For planetary applications, tunable laser spectrometers must therefore be miniaturized and robust. To maintain gas sensitivities, multipass optical cells are required. Typically, cell lengths of only 5–20 cm long can be accommodated, and cell diameters of up to only 5 cm or so. The Herriott cell configuration is chosen over the White cell configuration for reasons of optical and mechanical stability. Although superior sensitivity is possible using cavity ring-down techniques [12,13], this method requires mirrors of such high reflectivity (typically >99.9%) that a given set of mirrors are suitable only for a single wavelength, and the technique is much more demanding on stability compared with traditional multipass absorption (up to 100 passes). This means that for a six-wavelength spectrometer, six individual cells have to be made, a requirement that usually will break available mass or volume budgets.

Astigmatic variants of the Herriott cell can produce long effective path lengths. In 1965, Herriott and Schulte changed the pattern of reflections at the mirror surfaces from a circular–elliptical pattern to a Lissajous pattern with the introduction of astigmatic mirrors in their cell [14]. The circulating optical beam filled more of the volume of the cell and therefore, produced an increase in the total path length. Astigmatic cells with 484 passes have been achieved [15], but are usually designed for single laser injection. The simultaneous injection of several lasers into an astigmatic cell has several complications. The astigmatic cell is more difficult to align than a Herriott cell with spherical mirrors. The injection beam angle and rotational alignment of the astigmatic mirrors is crucial in the overall alignment of the cell. In addition, determining the potential locations for the injection and output holes are complicated by the distribution of the points of reflection on the mirrors.

B. Tunable Laser Spectrometer on the 2009 Mars Science Laboratory Mission

The JPL Tunable Laser Spectrometer (TLS; principal investigator C. R. Webster) has been selected as part of the Sample Analysis at Mars (SAM; PI Paul Mahaffy) analytical suite on the 2009 Mars Science Laboratory (MSL) mission. TLS will measure gas abundances (i) in the Martian atmosphere; (ii) adsorbed to soil; (iii) bound to rocks and released in pyrolysis experiments. Targeted gases are CH₄, H₂O, H₂O₂, N₂O, and CO₂. In addition, the isotope ratios of D/H in H₂O, ¹⁸O/¹⁷O/¹⁶O in H₂O and CO₂, and ¹³C/¹²C in CH₄ and CO₂ will be measured to better than 1%. TLS uses a simple multipass Herriott cell and four laser sources (near-IR, IC, and QC) covering the four channels at 2.64, 2.78, 3.27, and 7.8 μm (see Fig. 1).

TLS has a high sensitivity for gas detection. For example, for CH₄, TLS can measure the CH₄ abundance down to ten parts in 10¹² [0.01 parts per 10⁹ by volume (ppbv)] with preconcentration, or to sensitivities nearly 1000 times better than the recently observed amounts of 10–250 ppbv. Without precon-

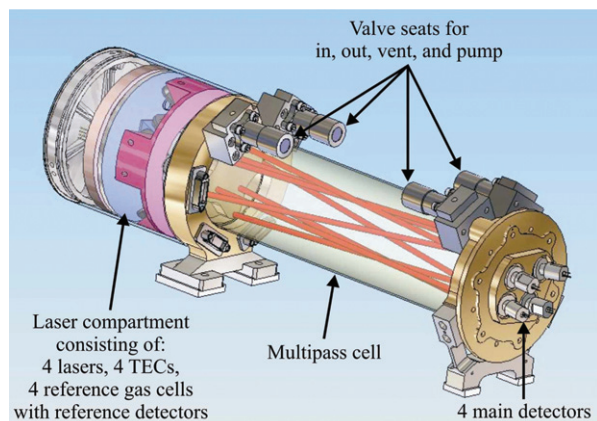


Fig. 1. TLS of the SAM analytical suite on the MSL mission.

centration, minimum detectable amounts of CH_4 are estimated to be ~ 1 ppbv, still ten times better than observed amounts. The preconcentration technique consists of chemically scrubbing the CO_2 from the sample and cold trapping the volatiles. The effect of preconcentration is to provide up to a 100-fold improvement in the sensitivity.

With the recent discovery of ~ 10 ppbv of CH_4 on Mars [16], much interest lies in its source, whether abiological (rock chemistry) or biological (methanogen production). One possible discriminator is the isotope ratio of $^{13}\text{C}/^{12}\text{C}$ in methane, since methanogens on Earth are known to produce CH_4 significantly depleted in the heavier isotope [17]. In addition to studying the diurnal, spatial, and seasonal variations of Martian methane to the parts in 10^{12} sensitivity, SAM will include sample preconcentration for TLS to measure the isotopic ratio $^{13}\text{C}/^{12}\text{C}$ in CH_4 for comparison with that measured in CO_2 (another channel). This will help assess the possible biogenic origin of CH_4 on Mars. Isotope ratios for many important gases will be made at precisions of typically a few parts per thousand.

C. Requirements for the Tunable Laser Spectrometer 2009 Mars Science Laboratory Instrument

Originally planned as a six-channel Herriott cell, the number of channels was trimmed down to four channels as a result of mission resource limitations. The additional two channels in the six-channel Herriott cell would increase the size of the electronics needed to operate these channels. The Herriott cell is re-

quired to be a compact (mirror separation of ~ 0.2 m) and low-volume (~ 400 cm³) cell that is capable of measuring molecular species whose concentration is on the order of parts in 10^9 .

The four-channel Herriott cell is designed for the simultaneous *in situ* measurement of five molecular species present within a single gas cell. Each individual laser channel follows its own optical path within the cell probing a particular molecular transition of interest. The total number of passes (81 passes) is tailored to achieve high sensitivity detection. Coating the mirror substrate with gold provides the reflectivity needed to obtain the optical throughput across the wavelength region. After a laser beam has circulated through the cell, the throughput of the cell is required to be 1–2 mW of laser radiation impinging on its corresponding detector. The wavelengths of the four lasers and the molecules of interest with their corresponding isotope ratios are presented in Table 1. Also presented in Table 1 is the limit of detection (LOD) for the molecules at a pressure of 10 mbar and a measurement interval of 100 s. The LODs, presented in Table 1, are limits without preconcentration of the sample gas. Both CH_4 and H_2O can undergo up to a 100-fold preconcentration providing a LOD of 10 parts per 10^{12} by volume (pptv) and 10 ppbv, respectively.

The Herriott cell possesses an intrinsic stability to small perturbations in the alignment. By constructing the cell and mirrors from an alloy that has a small coefficient of thermal expansion, the perturbations to the cell alignment will be minute over a large temperature range. An aluminum alloy, while having a slightly higher coefficient of thermal expansion, is preferred over Invar 36 and other high density alloys because of the mass budget constraints. Aluminum alloys are preferred over beryllium, even though beryllium has a coefficient of thermal expansion that is approximately a factor of 2 better than aluminum alloys. This preference is due to the difficulty associated with machining beryllium. Using an aluminum alloy will allow the cell to be operational over a temperature range of -40 to $+40$ °C with only small perturbations to the cell alignment.

2. Theoretical Background

A. Ray Propagation

The Herriott cell consists of two concave spherical mirrors, the near and far mirrors, separated by a

Table 1. TLS Laser Wavelengths, Target Gases, and Isotope Ratios

Laser Type	Wavelength (μm)	Target Gas	Target Isotopes Ratios	Limit of Detection ^a
NIR diode	2.64	H_2O	D/H , $^{18}\text{O}/^{16}\text{O}$, $^{17}\text{O}/^{16}\text{O}$	1 ppmv
NIR diode	2.78	CO_2	$^{13}\text{C}/^{12}\text{C}$, $^{18}\text{O}/^{17}\text{O}/^{16}\text{O}$	1 ppmv
IC	3.27	CH_4	$^{13}\text{C}/^{12}\text{C}$	1 ppbv
QC	7.8	H_2O_2 , N_2O	—	2 ppbv and 5 ppbv

^aLimit of detection without preconcentration at a pressure of 10 mbar and a 100 s measurement interval. Assumes second-harmonic detection of line center absorptions of 1×10^{-5} .

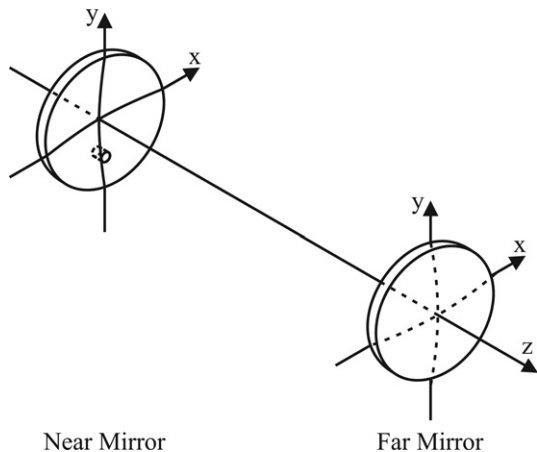


Fig. 2. Coordinate system of the Herriott cell showing near and far mirrors.

distance d . The coordinate system of the Herriott cell is shown in Fig. 2. The near and far mirrors are located at $z = 0$ and $z = d$, respectively. Both mirrors of the cell are centered at $x = y = 0$. The radius of curvature of the near and far mirrors are R_1 and R_2 , respectively.

An optical beam is injected in an off-axis direction into the Herriott cell through a coupling hole located in the near mirror. The beam propagates back and forth between the two mirrors before finally exiting through the coupling hole. As described later, it is not necessary to have the beam exit through the coupling hole; the beam can exit through another well-positioned hole in either the near or far mirrors. The propagation of the beam within the Herriott cell can be represented as a paraxial ray. The analysis of paraxial rays using geometric optics has been described before, and this section briefly presents some of the key concepts [18].

A propagating ray can be represented as a column vector $\mathbf{r} = [x, Sx, y, Sy]$, where x and y are the projected distances of the ray on the x and y axes with their corresponding slopes Sx and Sy , respectively. The transformation of \mathbf{r} , as the result of the ray propagating through free space or the intervention of an optic, occurs via a transfer matrix \mathbf{T} :

$$\mathbf{r}' = \mathbf{T}\mathbf{r}. \quad (1)$$

For the Herriott cell, the only transfer matrices that need to be considered are a ray propagating through free space and a ray reflecting off a concave spherical mirror. The transfer matrix for a ray propagating through free space is

$$\mathbf{T}(d) = \begin{bmatrix} 1 & d & 0 & 0 \\ 0 & 1 & 0 & 0 \\ 0 & 0 & 1 & d \\ 0 & 0 & 0 & 1 \end{bmatrix}. \quad (2)$$

The transfer matrix for a ray reflecting off a concave spherical mirror with radius of curvature R is

$$\mathbf{T}(R) = \begin{bmatrix} 1 & 0 & 0 & 0 \\ -2/R & 1 & 0 & 0 \\ 0 & 0 & 1 & 0 \\ 0 & 0 & -2/R & 1 \end{bmatrix}. \quad (3)$$

For one round trip in the Herriott cell, the transfer matrix is obtained from the free-space propagation $\mathbf{T}(d)$ and the mirror reflection $\mathbf{T}(R)$ matrices:

$$\mathbf{T} = \mathbf{T}(R_1)\mathbf{T}(d)\mathbf{T}(R_2)\mathbf{T}(d). \quad (4)$$

After n round trips, Eq. (1) can be rewritten as

$$\mathbf{r}_n' = \mathbf{T}^n \mathbf{r}. \quad (5)$$

B. Re-entrant Condition

When an off-axis ray is injected into the Herriott cell, the successive reflections of the ray map out an elliptical pattern at the points of reflection on the mirrors. The shape of the elliptical patterns on the mirrors is a function of the radius of curvature of the two mirrors, the separation of the mirrors, the position of the injected beam, and the injected beams angle. The equations presented by Herriott and co-workers provide an approximation to the circulation of the beams within the cell [14,19]. If the Herriott cell is treated as a spherical mirror interferometer under certain conditions, the ray will retrace its path within the cell; this is known as the re-entrant condition:

$$N\theta = 2M\pi. \quad (6)$$

The variable N , an even integer, is the total number of passes the beam makes within the cell. The integer M is the number of orbits the beam makes before exiting the cell. As shown in Fig. 3, the variable θ is the angle between two successive reflections, where

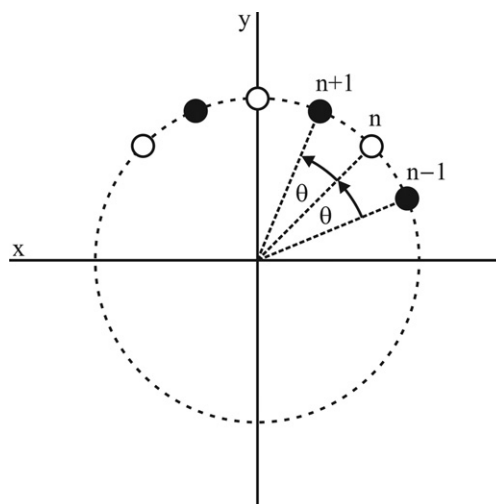


Fig. 3. Description of the angle θ as viewed looking down toward the positive z axis from the near mirror to the far mirror. The solid spots represent reflections on one mirror, whereas the circles represent reflections on the other mirror.

the n th point of reflection lies on one mirror and the $n + 1$ point of reflection lies on the other mirror. The angle between two successive points of reflection on one mirror is 2θ . Figure 3 shows the successive points of reflection orbit in a counterclockwise direction as viewed looking down the z axis from the near mirror to the far mirror. However, it is possible to have the successive points of reflection rotating in a clockwise direction for negative values of θ . To account for the sign of θ , Eq. (6) is rewritten as

$$N|\theta| = 2M\pi. \quad (7)$$

Herriott *et al.* showed that the mirror separation, the radius of curvature, and θ are related by [14,19]

$$\cos(\theta) = 1 - \frac{d}{R}. \quad (8)$$

For a given number of passes within a Herriott cell whose mirrors have a radius of curvature R , it is possible to have several solutions that satisfy both Eqs. (7) and (8) simultaneously. However, each one of these solutions differs slightly from each other in the pattern that is produced on the mirror surfaces from the points of reflection. To describe the differing patterns, the variables k and p are introduced. The integer variable k is defined as $k = \pm 2, \pm 4, \pm 6, \dots$ and p is a positive integer. The total number of passes in a Herriott cell is then

$$N = 2pM + k. \quad (9)$$

The patterns can be grouped in terms of families using Eq. (9). To avoid confusion, we represent families of solutions using Eq. (9) and a particular solution in a family using the notation $\{N, M, k, p\}$. For example, the family $N = 6M + 2$ contains the solutions $\{74, 12, +2, 3\}$, $\{80, 13, +2, 3\}$, and $\{86, 14, +2, 3\}$.

For mirrors with a given radius of curvature, the families of solutions can be further grouped according to their value of p . Figure 4 shows a graph of N versus

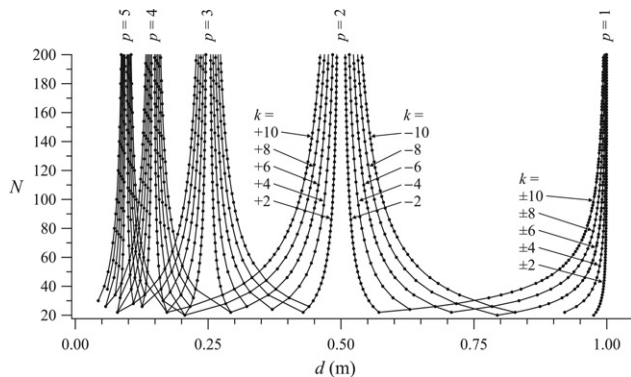


Fig. 4. Graph of N versus d for several families of solutions of a Herriott cell. The graph was calculated using a radius of curvature of 0.5 m for the spherical mirrors. Degenerate solutions have been removed from the plot.

d for solutions that take on values of $p = 1$ through $p = 5$ and $k = \pm 2$ through $k = \pm 10$. In this graph, the solutions are represented as dots. A particular family is represented as a line that intersects several solutions. The solutions presented in Fig. 4 were calculated using a radius of curvature of 0.5 m for both the near and far mirrors.

For each group of families with a particular value of p , the solutions approach an asymptotic limit $d_{p,M \rightarrow \infty}$. The asymptotic limit is determined from Eqs. (7)–(9) and evaluating the limit as M approaches infinity:

$$d_{p,M \rightarrow \infty} = \lim_{M \rightarrow \infty} \left(1 - \cos \left(\frac{2M\pi}{2pM + k} \right) \right) R. \quad (10)$$

As p increases, both $d_{p,M \rightarrow \infty}$ and the difference between two successive asymptotic limits ($d_{p+1,M \rightarrow \infty} - d_{p,M \rightarrow \infty}$) approach zero. For $p \neq 1$, the solutions with positive values of k will have $d < d_{p,M \rightarrow \infty}$ and the solutions with k possessing negative values will have $d > d_{p,M \rightarrow \infty}$.

For $p = 1$, the solutions will have $d < d_{p=1,M \rightarrow \infty}$ regardless of the sign of k . Additionally, the two solutions $\{N, M, +k, 1\}$ and $\{N, M + k, -k, 1\}$ will possess the same value for d . However, $\{N, M, +k, 1\}$ and $\{N, M + k, -k, 1\}$ will have different values of θ , $\theta_{p=1,M \rightarrow \infty} - \Delta\theta$ and $\theta_{p=1,M \rightarrow \infty} + \Delta\theta$, respectively, where $\theta_{p,M \rightarrow \infty}$ is the asymptotic limit of θ . The asymptotic limit $\theta_{p,M \rightarrow \infty}$ is defined similarly to $d_{p,M \rightarrow \infty}$. The families of solutions with a particular p approach an asymptotic limit in θ defined as $\theta_{p,M \rightarrow \infty}$. Using Eqs. (7) and (9), $\theta_{p,M \rightarrow \infty}$ is determined in the limit as M approaches infinity.

Figure 5 shows a graph of N versus θ for several solutions that have values of $p = 1$ through $p = 5$ and $k = \pm 2$ through $k = \pm 10$. The solutions presented in the graph of N versus θ were calculated using a radius of curvature of 0.5 m for both mirrors. The graph of N versus θ has several similarities to the graph of N versus d . As p increases, both $\theta_{p,M \rightarrow \infty}$ and the difference between two successive asymptotic limits ($\theta_{p+1,M \rightarrow \infty} - \theta_{p,M \rightarrow \infty}$) approach zero. The solutions with

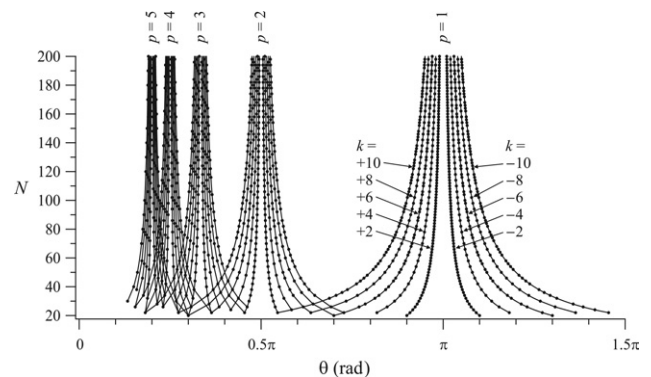


Fig. 5. N versus θ for several families of solutions of a Herriott cell. The graph was calculated using a radius of curvature of 0.5 m for the spherical mirrors. Degenerate solutions have been removed from the plot.

positive values of k have $\theta < \theta_{p,M \rightarrow \infty}$, and those families with negative values of k have $\theta > \theta_{p,M \rightarrow \infty}$.

Not all solutions to Eqs. (7) and (9) will be unique. When two solutions are degenerate, only one of the solutions will be obtained in the Herriott cell. Additionally, when two solutions are degenerate, the solutions will possess the same value for both d and θ . There are two types of degenerate solutions that can arise.

In the first type, two solutions may be degenerate that possess the same value of p . The two degenerate solutions will have the same value of θ and d ; however, the total number of passes will differ. These degenerate solutions are the result of a common factor present in Eq. (9) for the two solutions. The solution with the lower value of N will be obtained in the Herriott cell. For example, the solution {76, 12, 4, 3} is degenerate to the solution {38, 6, 2, 3}; both solutions have the same value of θ and d for a given radius of curvature. However, only the solution {38, 6, 2, 3} will be obtained in the Herriott cell. After reflection of the penultimate pass by the far mirror, the 38th pass will exit the cell via the coupling hole. A restriction is placed on M to ensure that a degenerate solution is not obtained. By restricting M such that $k'M(\text{mod } k) \neq 0$, where $k' < k$ and k' and k are even, a solution can be obtained that ensures there is not a degenerate solution [20]. For $k = \pm 4, \pm 6, \pm 8$, and ± 10 , M cannot be divisible by 2, 3, 2, and 5, respectively. When $k = \pm 2$, there is no restriction on M . The degenerate solutions of this type have been removed from Figs. 4 and 5 and only sustainable solutions have been shown.

The second type of degeneracy arises from solutions that have the same values for N and M , but differing values for k and p . This type of degeneracy is readily recognized with the aid of Figs. 4 and 5. Using these figures, the degeneracy appears as a solution that belongs to two different families, where each family has a different value of p . Equations (7) and (9) can be used to determine if there is a degenerate solution,

$$p + \frac{k}{2M} = p' + \frac{k'}{2M}, \quad (11)$$

where $k' < k$. If Eq. (11) is satisfied, then the two solutions are degenerate. The solution with the lower magnitude in k will be sustained in the cell. It is possible to have more than two degenerate solutions of this type. The solutions {28, 3, 10, 3}, {28, 3, 4, 4}, and {28, 3, -2, 5} are degenerate possessing the same value of θ and d for a given radius of curvature of the mirrors. However, only the solution {28, 3, -2, 5} will be obtained in the cell.

When $k = 0$, an interesting result is obtained. From Eqs. (7) and (9), setting $k = 0$ produces $\theta = \theta_{p,M \rightarrow \infty}$ and $d = d_{p,M \rightarrow \infty}$ for all N of a given p . For example, a Herriott cell with $R = 1.0$ m, all solutions $\{N, M, 0, 3\}$ will have $\theta = 60^\circ$ and $d = 0.5$ m. For a Herriott cell with the solution $\{N, M, 0, p\}$, the beam will exit

through the coupling hole after the p th point of reflection on the far mirror. The net result is a multipass cell where the total number of passes is equal to $2p$ regardless of the value of M .

C. Characteristics Patterns of Families of Solutions

The points of reflection from each family produce a characteristic spot pattern on the mirrors. For cells with a large value of N or those with poor mirror surface quality, understanding the pattern that is produced can aid in determining the total number of passes as well as aid in the alignment of the cell. As N increases, there is an increased difficulty in aligning the cell with the correct number of passes. As Figs. 4 and 5 show for large N , a small displacement in d and θ will result in obtaining the adjacent solution of a family. However, it was experimentally observed that for large N , only a small displacement in d was needed to produce a neighboring solution. This observation is attributed to the fact that the displacement needed in θ is small.

Figure 6 shows several solutions for a Herriott cell consisting of 82 passes. In this figure, the points of reflection on the far mirror are represented as spots. The spots are numbered according to their reflection, e.g., the first reflection is spot number 1, the third reflection is spot number 3, etc. Even numbered points of reflection occur on the near mirror. The size of the spot is a function of the intensity; for higher numbered points of reflection, the spot size is smaller. Each spot pattern is designated by its corresponding family, particular solution, θ , and d .

Some general trends in the appearance of the families can be made with the aid of Fig. 6. The value of p is the number of points of reflection per orbit on a mirror. Therefore, the spot numbers n and $n + 2$ are separated by an angular distance of approximately $2\pi/p$ rad, noting that $2\pi/p \approx 20$. As described earlier, the sign of θ dictates whether the 1st, 3rd, . . . , $n - 1$ points of reflection are circulating clockwise ($\theta < 0$) or counterclockwise ($\theta > 0$), as viewed along the z axis toward the surface of the far mirror. When viewed toward the surface of the near mirror, the points of reflection are circulating clockwise for $\theta > 0$ and counterclockwise for $\theta < 0$.

The sign of k dictates whether a full 2π rad orbit is made between the n th and $n + 2p$ point of reflection. Sweeping from the n th through the $n + 2, n + 4, \dots, n + 2p$ points of reflection when the sign of k is positive (negative), the angular difference between the n th and $n + 2p$ points of reflection is less (more) than 2π rad. The number of points of reflection between the n th and the $n + 2p$ points of reflection is determined by the magnitude of k and is $|k|/2 - 1$ points of reflection. When $k = \pm 2$, the n th and the $n + 2p$ points of reflection will be adjacent to each other.

The sign of k produces an intensity distribution for the points of reflection. The intensity distribution appears as a series of bands in the spot pattern on the mirrors. For $k = \pm 2$, the number of intensity bands present in the pattern is p . In Fig. 6, the solutions

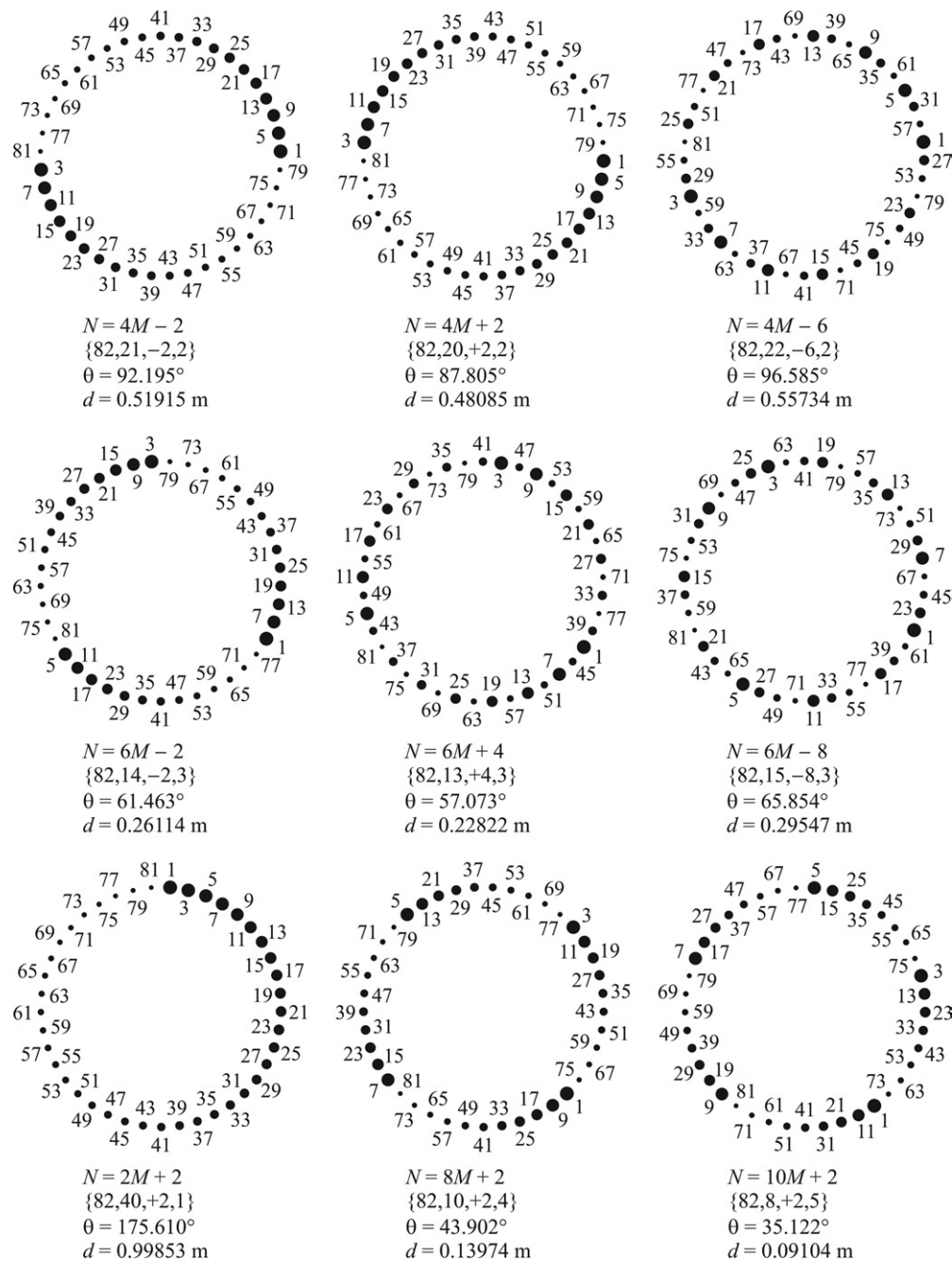


Fig. 6. Points of reflections on the far mirror for various solutions with $N = 82$. The spots are numbered according to the order of their reflection. The size of the spots is a function of the intensity, where the larger spots represent earlier reflections. The calculation was performed with a 0.5 m radius of curvature for the mirrors.

$\{82, 21, -2, 2\}$ and $\{82, 20, +2, 2\}$ clearly have two intensity bands, as compared with the solution $\{82, 14, -2, 3\}$, which has three intensity bands. The bands originate at the 1st, 3rd, \dots , $2p - 1$ points of reflection on the far mirror and the 0th, 2nd, \dots , $2p - 2$ points of reflection on the near mirror, where the 0th point is the injected beam. When $|k| \geq 4$, there appear to be subbands present within the bands.

When viewing the points of reflection on the surface of the far mirror, the intensity of the points of

reflection within each band decreases in a clockwise (counterclockwise) fashion when k is positive (negative), for $\theta > 0$. For $\theta < 0$ and when k is positive (negative), the intensity decreases in a counterclockwise (clockwise) fashion. When viewing the points of reflection on the surface of the near mirror, the intensity of the points of reflection within each band decreases in a clockwise (counterclockwise) fashion when k is negative (positive), for $\theta > 0$. For $\theta < 0$ and when k is positive (negative), the intensity decreases in a clockwise (counterclockwise) fashion.

For $k = \pm 2$, the intensity distribution appears smooth; but when $k \neq \pm 2$, the overall intensity directionality should be examined. For example, in Fig. 6, the solution $\{82, 22, -6, 2\}$ shows a series of subbands originating from the 1st, 5th, 9th, . . . , points of reflection on the surface of the far mirror; each subbands' intensity decreases in a clockwise manner. However, the overall intensity of the bands originating from the 1st and 3rd points of reflection decreases in a counterclockwise fashion as would be expected with $k = -6$.

Figure 7 consists of four black-and-white photos of the far mirror of a Herriott cell. Each photo shows the characteristic spot pattern for a particular solution with 82 passes. The first few reflections in the spot pattern are numbered accordingly. The dashed lines were added to the photo to emphasize the reflections of the first orbit on the far mirror; these reflections define the variable p . Note that the dashed lines also aid in the visual approximation of 2θ . In each of the photos, the radius of curvature of the near and far mirrors was 0.5 m.

Figure 7(a) shows the characteristic spot pattern for the solution $\{82, 21, -2, 2\}$. From this photo, it is evident that $p = 2$. The sign of k is negative because the angle between the 1st (n th) and the 5th ($n + 2p$) points of reflection, while sweeping through the 3rd ($n + 2$) point of reflection, is greater than 2π rad. The 1st (n th) and the 5th ($n + 2p$) points of reflection are adjacent to each other; therefore $|k| = 2$. The experimentally measured edge-to-edge mirror separation

was 0.5175 m, which agrees well with the calculated mirror separation of 0.51915 m.

Figure 7(b) shows the characteristic spot pattern for the solution $\{82, 20, +2, 2\}$. The measured edge-to-edge mirror separation and calculated mirror separations were 0.4790 m and 0.48085 m, respectively. Figures 7(c) and 7(d) show the solutions $\{82, 14, -2, 3\}$ and $\{82, 13, +4, 3\}$, with measured edge-to-edge (and calculated) mirror separations of 0.2595 m (0.26114 m) and 0.2275 m (0.22822 m), respectively. The photos in Fig. 7 agree well with the calculated spot patterns presented in Fig. 6.

Understanding the characteristic spot patterns generated by each family can aid in the alignment of the Herriott cell. A simple observation of the pattern reveals the family of the pattern as well as the particular solution. For Herriott cells that possess a large number of passes or poor mirror surface quality, the spot pattern produced on the mirrors can aid in determining the total number of passes.

3. Prototype Cells

A. Design Considerations

The design of the Herriott cell for the TLS package required that several considerations be addressed in addition to those stated earlier. The Herriott cell was required to be a compact (mirror separation of ~ 0.2 m) and low volume (~ 400 cm³) cell that is capable of producing a path length (~ 16 m) suitable to measure in the tens of parts per 10⁹ or better using wavelength modulated lasers. By specifying the mirror separation, a Herriott cell solution $\{N, M, k, p\}$ and the radius of curvature of the mirrors can be tailored to accommodate the specified mirror separation. The size of the mirrors is also an important consideration. The mirrors should be large enough, such that the spot pattern can be spread out over the mirror to reduce spillover from the reflections that neighbor the input and output holes.

The Herriott cell was to be multiplexed with several lasers for the simultaneous *in situ* measurement of several molecular species. Each of the lasers could be injected into one coupling hole as was done in the SPIRALE instrument [21]. However, to accommodate all of the lasers and detectors, the lasers/detectors would need to be placed substantially far away from the back of the near mirror, thus increasing the overall size of the spectrometer. Another alternative is to have each laser injected into the cell via its own injection hole as done on the ALIAS instrument [22]. In this instrument, the beams from four diode lasers are injected into the Herriott cell via their own coupling holes. The ALIAS Herriott cell is configured for the $\{80, 13, +2, 3\}$ solution using a radius of curvature of 2.0942 m for the mirrors and a mirror separation of 1.0 m. Each hole is placed at different distances from the mirror center and all of the holes are aligned along the y axis. The size of the ALIAS mirrors is relatively large (15.24 cm diameter) as compared with the size required for the Herriott cell of the TLS package (~ 5.08 cm diameter). Smaller mirrors incor-

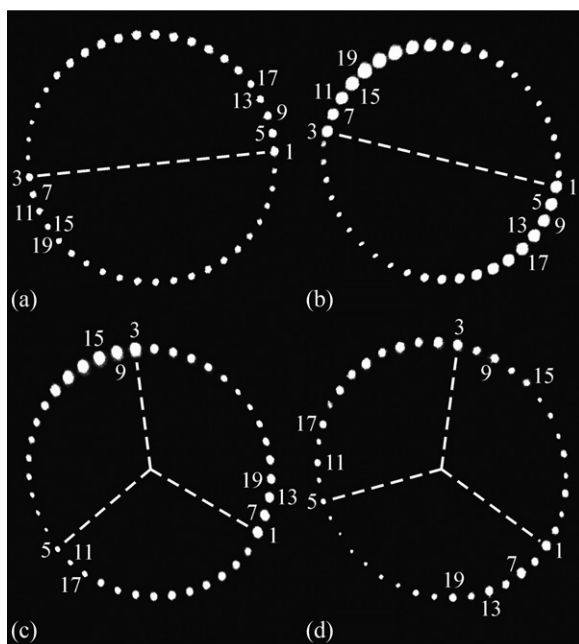


Fig. 7. Black and white photos of the far mirror of a Herriott cell showing several characteristic spot patterns for different solutions. The radius of curvature of the near and far mirrors was 0.5 m. The Herriott cell consisted of 82 passes with the solutions (a) $\{82, 21, -2, 2\}$, (b) $\{82, 20, +2, 2\}$, (c) $\{82, 14, -2, 3\}$, and (d) $\{82, 13, +4, 3\}$.

porated into the ALIAS configuration would decrease the spacing between the points of reflection on the mirrors. As a result, there would be a larger degree of spillover from the points of reflection that neighbor the coupling holes; this would be especially true for holes located closer to the mirror center. Additionally, in earlier prototypes for the Herriott cell of the TLS package, different Herriott solutions could be obtained when the holes were not located equidistant from the mirror center. These different Herriott solutions were attributed to the separation between the mirrors decreasing with increasing distance from the center of the mirror due to the radius of curvature. This is not observed on the ALIAS cell because the radius of curvature of the mirrors is substantially larger and the neighboring Herriott solutions require a larger offset to the specified mirror separation.

To obtain the same Herriott solutions for each of the laser channels, each of the injection holes needs to be equidistant from the mirror center. Spillover from the beam of one laser into another laser channel hole is avoided by changing the spot pattern from a circular pattern to an elliptical pattern. An elliptical pattern is produced by altering the angle of the injected beam and thereby permitting the injection holes to lie on a radius from the mirror center.

By designing a Herriott cell with separate input and output holes as opposed to one coupling hole, the overall size of the spectrometer can be reduced. In a typical Herriott cell, a laser injects a beam into the cell through a coupling hole. The beam reflects back and forth between the mirrors, eventually exiting through the coupling hole. In this configuration, the angle between the injected beam and the output beam is typically small. To resolve the output beam from the injected beam, the laser and detector are placed at a reasonable distance from the back of the near mirror. To produce a more compact spectrometer, the output holes of each laser channel are strategically placed in the far mirror, thus allowing the detectors and the lasers to be placed close to the backside of the far and near mirrors, respectively. The output holes could have been placed in the near mirror; consequentially, there was the potential issue of overcrowding between the lasers and detectors.

The choice for the locations of the output holes were dependent on the particular Herriott cell solution $\{N, M, k, p\}$. This choice encompasses the total path length as well as the effects of interference fringes. McManus and Kebabian demonstrated that the interference fringe free spectral range (FSR) is dependent on the families of solutions [20]. They observed interference fringes related to the path length of the points of reflection that neighbor the coupling hole for the families $N = 4M \pm 2$ and $N = 4M \pm 4$. Recasting their equations to incorporate the variable p , the neighboring points of reflection are $(2p)$ and $(N - 2p)$, for families of solutions with $k = \pm 2$, and $(N/2 - p)$ and $(N/2 + p)$ for $k = \pm 4$. These solutions for the neighboring points of reflection are for a Herriott cell where the injected and output beams pass through the same hole. For a cell with separate in-

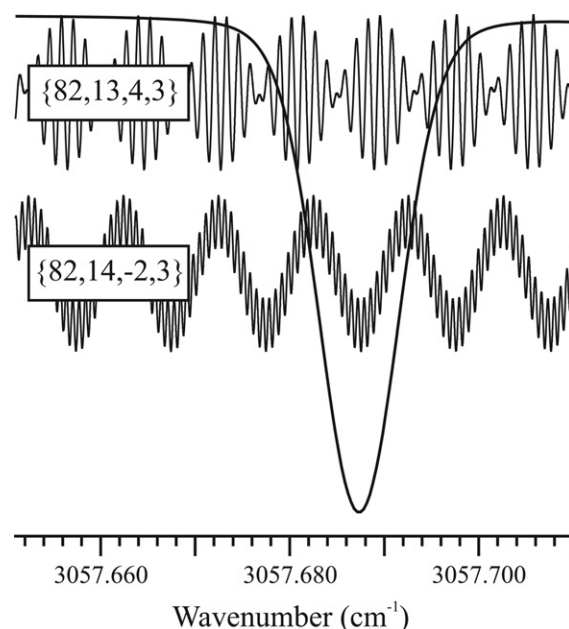


Fig. 8. Simulated interference fringes for the $\{82, 13, 4, 3\}$ and $\{82, 14, -2, 3\}$ solutions of a Herriott cell with the 81st pass removed. Overlaid is a simulated $A_1(1)$ line of the $R(3)$ multiplet of the ν_3 band of CH_4 . The CH_4 line was calculated using Hitran with a pressure of 7 mbar and a temperature of 280 K.

jection and output holes, the relationship is more complicated and a spot pattern diagram should be generated for verification of the neighboring points of reflection.

The simulated interference fringes from the $\{82, 14, -2, 3\}$ and $\{82, 13, 4, 3\}$ solutions are compared in Fig. 8. In this figure, the simulated interference fringes from the extraction of the 81st pass by an output hole placed in the far mirror are shown. Included in this figure, there is a simulated $A_1(1)$ line of the $R(3)$ multiplet of the ν_3 band of CH_4 . The CH_4 line was calculated using Hitran with a pressure of 7 mbar and a temperature of 280 K. For each solution, there are two fringe periods that correspond to the path lengths of the neighboring reflections. The points of reflection that neighbor the output hole are reflection numbers 5 and 75 for the $\{82, 14, -2, 3\}$ solution and reflection numbers 37 and 43 for the $\{82, 13, 4, 3\}$ solution. In the $\{82, 14, -2, 3\}$ solution, there are low-frequency fringes ($\text{FSR } \Delta\nu = 0.0100 \text{ cm}^{-1}$) associated with five passes and high-frequency fringes ($\text{FSR } \Delta\nu = 0.0007 \text{ cm}^{-1}$) corresponding to 75 passes. While it is possible to filter out the high-frequency fringes, the low-frequency fringes have a FSR approximately equal to the line width of CH_4 ($\Delta\nu \sim 0.011 \text{ cm}^{-1}$ FWHM). Therefore, it is not possible to filter out the low-frequency fringes. There are two fringe periods for the $\{82, 13, 4, 3\}$ solution. However, the FSR of the fringes are fairly close, 0.0013 and 0.0011 cm^{-1} for the 37th and 43rd passes, respectively. Because the periods of the two fringes are close, there is a periodic decrease in the overall fringe amplitude. Nevertheless, the overall frequency

of the fringes from the {82, 13, 4, 3} solution is high enough to be filtered.

B. Cell Designs: Four- and Six-Laser Channel Herriott Cells

Two Herriott cells, a four-laser and a six-laser channel, were designed and constructed using the model described earlier. Both Herriott cells were designed using the solution {82, 13, 4, 3}. Separate injection holes were placed in the near mirrors to allow each laser beam to enter the cells individually. After the beams circulated between the near and far mirrors, the 81st pass was removed from each channel via output holes located in the far mirrors of both Herriott cells.

Figure 9 shows the spot patterns for both the four- and six-laser channel Herriott cells. Each color in Fig. 9 represents the points of reflection for one particular

laser channel; each laser channel is labeled Laser 1, Laser 2, etc. . . . The injection and output holes in the near and far mirrors, respectively, are designated as small circles. In this figure, the points of reflection on the near and far mirror are represented as spots. The spot size is a function of the intensity; as the number of reflections of a beam increases, the spot size decreases. Additionally, the injected and output beams are represented as spots; the injected beams have the largest spot size and the output beams have the smallest spot size. As seen in this figure, cross talk, the beam from one laser spilling over into the output hole of another laser, may be a potential issue. However, any cross talk that may be present can be reduced or eliminated using properly coated optics placed behind the far mirror and between the output holes and the detectors.

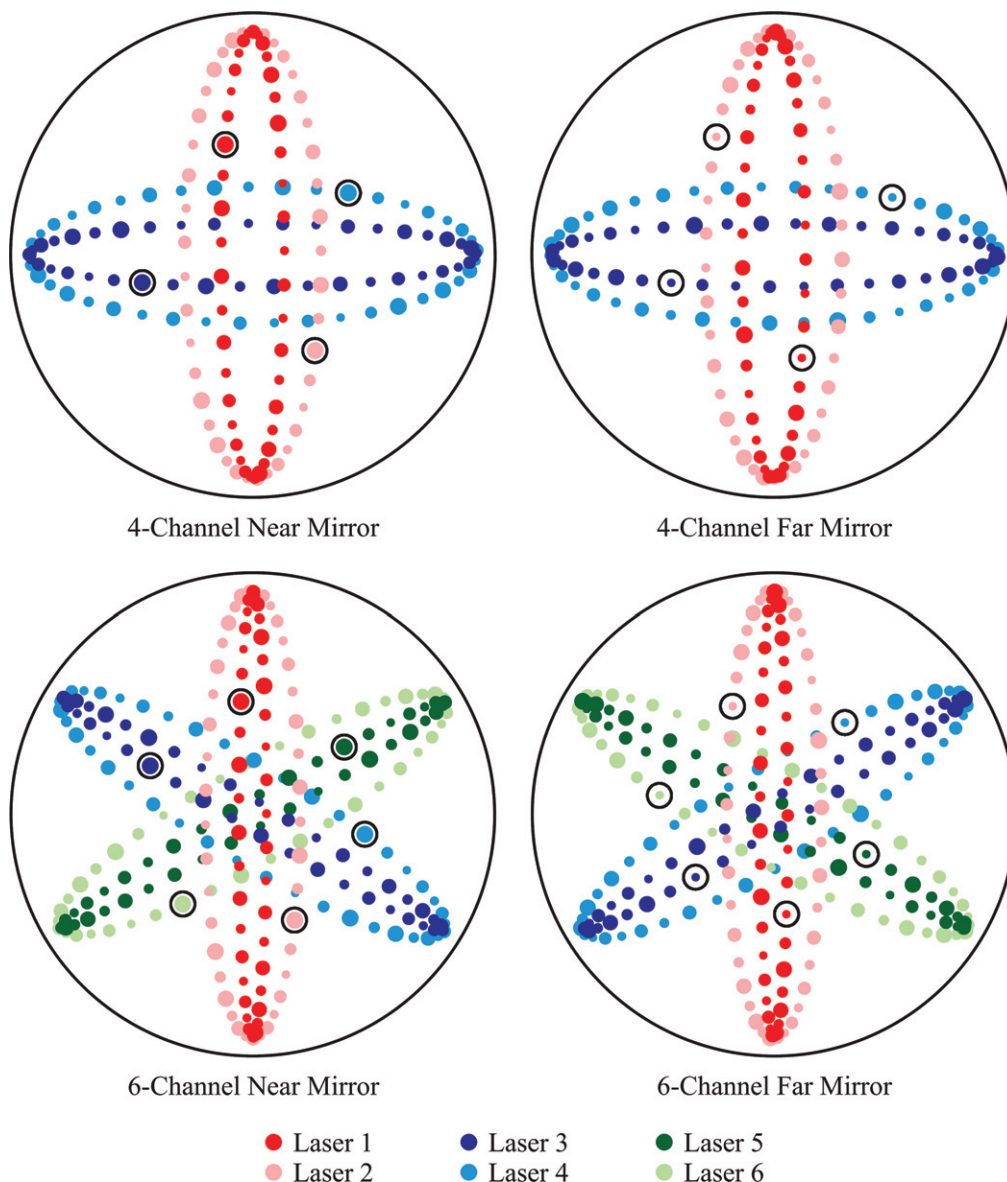


Fig. 9. Points of reflections on the near and far mirrors of a four-channel and a six-channel Herriott cell as viewed toward the mirror surfaces. Each color represents a different laser channel. The circles on the near mirror represent the laser injection holes. The circles on the far mirror represent the beam output holes, where the 81st pass is removed from the cell. The spot size is a function of the beam intensity.

The spot pattern for the six-laser channel Herriott cell consists of a narrow ellipse (Laser 1) centered within a wider ellipse (Laser 2). Viewing toward the surface of the near mirror, the spot patterns for Lasers 1 and 2 are rotated to produce the spot patterns for the remaining four laser channels. In addition to the interference fringes associated with the 37th and 43rd passes, Lasers 1, 3, and 5 in the six-laser channel version may exhibit interference fringes from the 3rd and 41st passes. This is a result of the tightness of the ellipses that brings the 3rd and 41st points of reflection in close proximity to the output holes. The widths of the elliptical spot patterns for Lasers 1, 3, and 5 can be increased to reduce the intensity of the additional interference fringes; however, care must be taken to avoid cross talk.

A prototype of the six-channel Herriott cell was constructed using commercially available spherical mirrors. The radius of curvature was 0.5 m for both the near and far mirrors. The mirror substrate was pyrex and coated with protected silver. The mirrors had a specified average reflectivity of $>96\%$ from 480–1100 nm. Holes were drilled orthogonal to the plane of the mirrors using a diamond-tipped drill bit. The holes were tapered from the backside of the mirrors. The tapered angle was chosen such that the injected beams would pass through the injection holes of the near mirror without clipping the mirror substrate and probe the entire surface of the far mirror. Tapering the holes from the backside of the far mirror allowed the output beams to clear the mirror substrate upon exiting the cell.

Figure 10 shows a color photograph of the far mirror of the six-laser channel Herriott cell. The radiation source consisted of three diode lasers operating

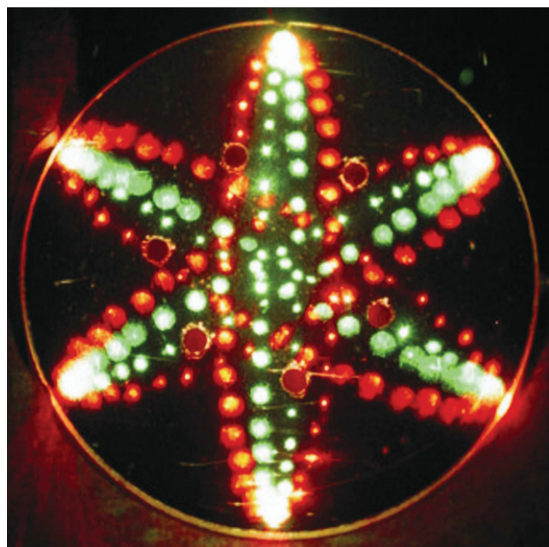


Fig. 10. Color photograph of the far mirror of a six-channel Herriott cell. The holes in the far mirror are the output hole that removed the 81st pass from each channel. The channels for Lasers 1, 3, and 5 used a 532 nm diode lasers for the radiation source. The channels for Lasers 2, 4, and 6 used 632 nm HeNe lasers.

at 532 nm and three HeNe lasers operating at 632 nm. The beams from the 532 nm diode lasers were injected through the injection holes for Lasers 1, 3, and 5. The beams from the HeNe lasers were injected through the injection holes for Lasers 2, 4, and 6. The radius of curvature of the mirrors was 0.5 m, and the experimentally measured edge-to-edge mirror was 0.2269 m.

The spot pattern for the four-channel version consists of four ellipses. A narrow ellipse (Laser 1) is centered within a wider ellipse (Laser 2). This pattern is then rotated to obtain Lasers 3 and 4. The elliptical spot patterns in this version are slightly wider than in the six-laser channel version. Opening the spot patterns has the benefit of reducing the contributions to the interference fringes associated with the 3rd and 41st passes. In the four-laser channel version, the 3rd and 41st points of reflection are approximately twice as far away from the output hole than in the six-laser channel version. Additionally, the reduction in interference fringes associated with the 3rd and 41st passes is accomplished without contributing any additional cross talk, because the points of reflection from one laser channel that neighbor the output hole from another laser channel are further away.

Figure 11 shows the front and back of the near and far mirrors of the four-laser channel prototype. The mirrors for the four-laser channel prototype cell were diamond turned from aluminum and coated with a protected gold coating. The center portion of the mirrors is the optical active area. The area that surrounds the active area was machined parallel to the plane of the mirrors. This outer area of the mirror rests on an o-ring of a cylindrical laboratory cell that is under vacuum. The backs of the mirrors contain a recess for an antireflection coated wedged window.



Fig. 11. Color photograph of the front and back of the near and far mirrors of the four-laser channel Herriott cell prototype. The near mirror is shown on the left. The far mirror is shown on the right.

Within this window recess, there is an o-ring groove that seals the window to the mirror substrate when under vacuum. The backs of the mirrors were drilled with #4–40 threaded holes that allow the mirrors to be removed from the vacuum cell. In addition, these threaded holes were used to rotationally align the near and far mirrors. In the four-laser channel prototype, tapered holes were machined orthogonal to the plane of the mirrors, similar to the six-laser channel prototype. The parameters for the radius of curvature of the mirrors and the separation between the mirrors for the four-laser channel prototype are currently controlled by International Traffic in Arms Regulations (ITAR) and Export Administration Regulations (EAR). However, these parameters were chosen such that the design considerations presented earlier were met.

Earlier studies on the four-laser channel Herriott cell used HeNe lasers operating at 632 nm as the radiation source. Small changes in the mirror separation can cause the next Herriott solution to occur in the cell as described in Figs. 4 and 5; this occurs only if the output beam of that particular solution coincidentally passes through the output hole. For the four-laser channel Herriott cell, the solutions {70, 11, 4, 3} and {94, 15, 4, 3} can occur to produce a cell with 69 and 93 passes, respectively. However in between these solutions, it is possible to obtain a cell with the total number of passes equal to the point of reflection that neighbors the output hole. This is a result of the points of reflection rotating within the elliptical spot pattern as the separation between the mirrors is changed. For the four-laser channel prototype, the 37th and 43rd points of reflection neighbor the output hole. As the mirror separation is changed, it is possible to obtain cells with 37 and 43 passes. However, these are not pure solutions; these path lengths occur when a point of reflection falls into the output hole as the separation between the mirrors is changed.

4. Conclusion

Geometric optics and matrix methods were used to mathematically describe a spherical mirror Herriott cell. The variables k and p were introduced to categorize the solutions of the Herriott cell in terms of families. Not all solutions to the Herriott cell are unique and degenerate solutions were described in detail. A characterization of the families of solutions and the differing spot patterns visible on the mirror surfaces was presented.

Four- and six-laser Herriott cells have been modeled and designed using geometric optics and matrix methods. Each individual laser channel followed its own optical path within the cell. Strategically placed output holes located in the far mirrors reduced the size of the spectrometers. The compact, multichannel Herriott cells were designed for the simultaneous *in situ* measurement of several molecular gases present within a single gas cell.

The four-channel Herriott cell configuration is presented as part of the design basis for the Jet Propulsion Laboratory TLS instrument (PI Webster)

selected for the SAM analytical suite (PI Mahaffy) on the MSL mission. TLS will measure gas abundances in the atmosphere of Mars, adsorbed in soil, and bound to rocks that are released during pyrolysis experiments. The four-channel Herriott cell will use four laser sources operating in the near-IR and IR wavelength regions. The four laser channels operate at 2.64, 2.78, 3.27, and 7.8 μm while using near-IR diode, IC, and QC lasers as the radiation sources. The target gases and their corresponding limits of detection of TLS are CH_4 at 1 ppbv, H_2O at 1 ppmv, H_2O_2 at 2 ppbv, N_2O at 5 ppbv, and CO_2 at 1 ppmv. To improve the sensitivity, preconcentration can be used to provide a limit of detection for CH_4 and H_2O of up to 10 pptv and 10 ppbv, respectively. In addition to measuring absolute concentrations, TLS will measure the isotope ratios of D/H in water, $^{18}\text{O}/^{17}\text{O}/^{16}\text{O}$ in water and carbon dioxide, and $^{13}\text{C}/^{12}\text{C}$ in methane and carbon dioxide.

This research was performed at the Jet Propulsion Laboratory, California Institute of Technology, under contract with the National Aeronautics and Space Administration. This research was performed while Christopher Tarsitano held a National Research Council Research Associateship Award at the Jet Propulsion Laboratory. The authors thank Chuck Devereese and the team at Lightwave Enterprises for manufacturing several mirror prototypes of the four-channel Herriott cell design. We also thank Jeff Hoffman, Mike Rodgers, and Tim McGuire of Optical Research Associates for their continued work on developing a Gaussian model and optical specifications for the flight instrument version of the four-channel Herriott cell for the TLS.

References

1. C. R. Webster, R. T. Menzies, and E. D. Hinkley, "Infrared laser absorption: theory and applications," *Laser Remote Chemical Analysis*, R. M. Measures, ed. (Wiley, 1988), Chap. 3.
2. J. Faist, F. Capasso, D. L. Sivco, C. Sirtori, A. L. Hutchinson, and A. Y. Cho, "Quantum cascade lasers," *Science* **264**, 553–555 (1994).
3. C. Gmachl, F. Capasso, J. Faist, A. L. Hutchinson, A. Tredicucci, D. L. Sivco, J. N. Baillargeon, S. N. G. Chu, and A. Y. Cho, "Continuous-wave and high power pulsed operation of index-coupled distributed feedback quantum cascade laser at $\lambda \approx 8.5 \mu\text{m}$," *Appl. Phys. Lett.* **72**, 1430–1432 (1998).
4. A. Evans, J. Nguyen, S. Slivken, J. S. Yu, S. R. Darvish, and M. Razeghi, "Quantum-cascade lasers operating in continuous-wave mode above 90 °C at $\lambda \sim 5.25 \mu\text{m}$," *Appl. Phys. Lett.* **88**, 051105 (2006).
5. J. S. Yu, S. Slivken, S. R. Darvish, A. Evans, B. Gokden, and M. Razeghi, "High-power, room-temperature, and continuous-wave operation of distributed-feedback quantum-cascade lasers at $\lambda \sim 4.8 \mu\text{m}$," *Appl. Phys. Lett.* **87**, 041104 (2005).
6. R. Q. Yang, "Infrared laser based on intersubband transitions in quantum wells," *Superlattices Microstruct.* **17**, 77–83 (1995).
7. J. R. Meyer, I. Vurgaftman, R. Q. Yang, and L. R. Ram-Mohan, "Type-II and type-I interband cascade lasers," *Electron. Lett.* **32**, 45–46 (1996).
8. R. Q. Yang, C. J. Hill, B. H. Yang, R. E. Muller, and P. M. Echternach, "Continuous-wave operation of distributed feed-

- back interband cascade lasers,” *Appl. Phys. Lett.* **84**, 3699–3701 (2004).
9. R. Q. Yang, C. J. Hill, and B. H. Yang, “High-temperature and low-threshold midinfrared interband cascade lasers,” *Appl. Phys. Lett.* **87**, 151109 (2005).
 10. W. W. Bewley, J. A. Nolde, D. C. Larrabee, C. L. Canedy, C. S. Kim, M. Kim, I. Vurgaftman, and J. R. Meyer, “Interband cascade laser operating cw to 257 K at $\lambda = 3.7\ \mu\text{m}$,” *Appl. Phys. Lett.* **89**, 161106 (2006).
 11. K. Mansour, Y. Qiu, C. J. Hill, A. Soibel, and R. Q. Yang, “Mid-infrared interband cascade lasers at thermoelectric cooler temperatures,” *Electron. Lett.* **42**, 31 (2006).
 12. M. D. Wheeler, S. M. Newman, A. J. Orr-Ewing, and M. N. R. Ashford, “Cavity ring-down spectroscopy,” *J. Chem. Soc. Faraday Trans.* **94**, 337–351 (1998).
 13. G. Berden, R. Peeters, and G. Meijer, “Cavity ring-down spectroscopy: experimental schemes and application,” *Int. Rev. Phys. Chem.* **19**, 565–607 (2000).
 14. D. R. Herriott and H. J. Schulte, “Folded optical delay lines,” *Appl. Opt.* **4**, 883–889 (1965).
 15. J. B. McManus, P. L. Kebabian, and M. S. Zahniser, “Astigmatic mirror multipass absorption cells for long-path-length spectroscopy,” *Appl. Opt.* **34**, 3336–3348 (1995).
 16. V. A. Krasnopolsky, J. P. Maillard, and T. C. Owen, “Detection of methane in the martian atmosphere: evidence for life?” *Icarus* **172**, 537–547 (2004).
 17. C. R. Webster, “Measuring methane and its isotopes $^{12}\text{CH}_4$, $^{13}\text{CH}_4$, and CH_3D on the surface of Mars with *in situ* laser spectroscopy,” *Appl. Opt.* **44**, 1226–1235 (2005).
 18. H. Kogelnik and T. Li, “Laser beams and resonators,” *Appl. Opt.* **5**, 1550–1567 (1966).
 19. D. Herriott, H. Kogelnik, and R. Kompfner, “Off-axis paths in spherical mirror interferometers,” *Appl. Opt.* **3**, 523–526 (1964).
 20. J. B. McManus and P. L. Kebabian, “Narrow optical interference fringes for certain setup conditions in multipass absorption cells of the Herriott type,” *Appl. Opt.* **29**, 898–900 (1990).
 21. G. Moreau, C. Robert, V. Catoire, M. Chartier, C. Camy-Peyret, N. Huret, M. Pirre, L. Pomathiod, and G. Chalumeau, “SPIRALE: a multispecies *in situ* balloonborne instrument with six tunable diode laser spectrometers,” *Appl. Opt.* **44**, 5972–5989 (2005).
 22. C. R. Webster, R. D. May, C. A. Trimble, R. G. Chave, and J. Kendall, “Aircraft (ER-2) laser infrared absorption spectrometer (ALIAS) for *in situ* stratospheric measurements of HCl , N_2O , CH_4 , NO_2 , and HNO_3 ,” *Appl. Opt.* **33**, 454–472 (1994).